

# Signature of quantum magnetism in thick rhombohedral graphite

Imre Hagymási<sup>2, 6, 7, 8 †</sup>, Mohammad Syahid Mohd Isa<sup>1, †</sup>, Zoltán Tajkov<sup>1, 5</sup>,  
Krisztián Máriy<sup>1</sup>, Oroszlány László<sup>3, 4</sup>, János Koltai<sup>5</sup>, Assem Alassaf<sup>3</sup>, Péter  
Kun<sup>1</sup>, Konrád Kandrai<sup>1</sup>, András Pálinkás<sup>1</sup>, Péter Vancsó<sup>1</sup>, Levente Tapasztó<sup>1</sup>,  
and Péter Nemes-Incze<sup>1, \*</sup>

<sup>1</sup>Centre for Energy Research, Institute of Technical Physics and Materials  
Science, 1121 Budapest, Hungary

<sup>2</sup>Helmholtz-Zentrum Berlin für Materialien und Energie, 14109 Berlin, Germany

<sup>3</sup>Department of Physics of Complex Systems, ELTE Eötvös Loránd University,  
1117 Budapest, Hungary

<sup>4</sup>Budapest University of Technology and Economics, 1111 Budapest, Hungary

<sup>5</sup>ELTE Eötvös Loránd University, Department of Biological Physics, 1117  
Budapest, Hungary

<sup>6</sup>Wigner Research Centre for Physics, 1121 Budapest, Hungary

<sup>7</sup>Dahlem Center for Complex Quantum Systems and Institut für Theoretische  
Physik, Freie Universität Berlin, 14195 Berlin, Germany

<sup>8</sup>Max Planck Institute for the Physics of Complex Systems, Dresden, Germany

<sup>†</sup>*These authors contributed equally*

*\* corresponding author, email: nemes.incze.peter@ek-cer.hu*

January 27, 2022

In low-dimensional quantum magnets antiferromagnetic exchange between spins results in an exceptionally rich behavior with significance from spintronics to high temperature superconductivity. Their theoretical models are simple to formulate, such as the Haldane spin chain, but condensed matter realizations are found in binary, ternary or even more complex compounds, making the realization of defect free materials difficult. Here we show that, one of the simplest compounds, thick rhombohedral graphite (RG) shows signatures of quantum magnetism below 20 Kelvin. By scanning tunneling microscopy we map the surface state charge density of 8 and 10 layers and identify a domain structure emerging from a competition between a sublattice antiferromagnetic insulator and a gapless correlated paramagnet, forming the hallmark degeneracy of a quantum magnet ground state. We perform density-matrix renormalization group calculations, explaining the observed features and demonstrate that the mean-field sublattice-Néel antiferromagnet is not the ground state, just as expected for a quantum magnet. Thick RG offers a simple and tunable materials platform to explore magnetism beyond the mean-field approximation, in a system with itinerant spins.

An important factor separating conventional and quantum magnets is that in the latter the mean-field description fails due to strong correlations and quantum fluctuations. Examples include antiferromagnetic spin chains<sup>1</sup> and ladders<sup>2</sup>, where strong interactions result in exotic properties such as fractionalization and topological order<sup>3</sup>. Generally, condensed matter systems realizing quantum magnets have a complex structure, requiring the spins provided by the  $d$ -band of transition metals<sup>4</sup>. On the other hand, graphene based materials comprising only carbon atoms are simple and host a remarkable multitude of magnetic states, provided that a band with a divergent charge density is partially filled. This divergence can arise through a sublattice imbalance<sup>5-9</sup>, a Landau level<sup>10;11</sup>, or in a moiré superlattice<sup>12;13</sup>. Perhaps the simplest example of this is at the edges of zigzag nanoribbons, where at charge neutrality<sup>14</sup>, the spins on opposite sublattices interact antiferromagnetically<sup>5</sup>. Further examples are in the layer antiferromagnet state of bilayer graphene<sup>9;15;16</sup> and in the sublattice-Néel state in trilayer<sup>17-19</sup> and tetralayer RG<sup>20-22</sup>. This Néel state has the spins on opposing sublattices in an antiparallel configuration between the top and bottom surface and in a ferrimagnetic orientation within the

same graphene layer. Mean-field Hubbard models predict it to be the gapped ground state at charge neutrality, measured in three and four layer RG by transport<sup>17</sup> and STM<sup>22</sup>. However, for thicker RG interactions are expected to increase<sup>23</sup>, holding the potential for driving a transition to a quantum magnet, providing the first realization of graphene based magnetism beyond the mean-field model.

Here we show that for thick RG, the gapped Néel state is not the ground state, because fluctuation terms and local correlations can not be neglected. Instead, RG hosts domains of alternating gapped and gapless surface charge density, associated with a degenerate ground state. This degeneracy is a signature of quantum magnetism<sup>3</sup> that can not be described at the mean-field level.

RG is distinct from any other graphene system in that it features a staggered intra and inter-layer hopping pattern<sup>24</sup>, similar to a 1D Su-Schrieffer-Heeger model<sup>25</sup>. It can be considered as built up from parallel SSH chains (Fig. 1a) leading to a sublattice imbalance on the top and bottom surfaces. A flat band is localized on the unpaired surface sublattice (blue in Fig. 1a), which decays into the bulk<sup>26;27</sup>. The interacting 1D SSH chain<sup>28;29</sup> and "ladder materials"<sup>2</sup> with the chains linked up parallel to each other are elementary models for quantum magnets. This, together with the recent evidence for strong correlations in thick samples<sup>30</sup> make RG a prime candidate for quantum magnetism.

Scanning tunneling microscopy (STM) is a powerful tool to investigate correlated electron systems, for example uncovering the inhomogeneities in the order parameter of high  $T_C$  superconductors<sup>31</sup>, or nematicity in "magic-angle" bilayer graphene<sup>32-35</sup>. We present STM measurements at a temperature of 9.6 K, on the surface of SiO<sub>2</sub> supported RG (Fig. 1a). At half filling of the flat band (charge neutrality) two distinct phases of the surface state charge density appear. One having a splitting of up to 40 meV centered on the Fermi level, the other state being gapless. The two phases form a domain structure, characteristic of many-body competing ground states<sup>31</sup>. Using density matrix renormalization group (DMRG) calculations, we identify that the surface hosts a net spin of  $\mathcal{S} = 1$ . This magnetic moment gives rise to a ground state of RG, that has the degenerate spin projections on the surface of:  $s_z = \pm 1$  and  $s_z = 0$ . The  $s_z = \pm 1$  surface state corresponds to the sublattice-Néel insulator, identified earlier using mean-field approaches: ab-initio<sup>23</sup>, Hubbard<sup>17</sup>, Hartree-Fock<sup>36</sup> and continuum model<sup>37</sup> calculations. The

$s_z = 0$  surface state is a correlated paramagnet, that is not present at the mean-field level<sup>17;36</sup>. The degeneracy between the gapless paramagnetic state and the antiferromagnetic insulator is an intrinsic property of RG and explains the domain structure of the surface state splitting observed experimentally.

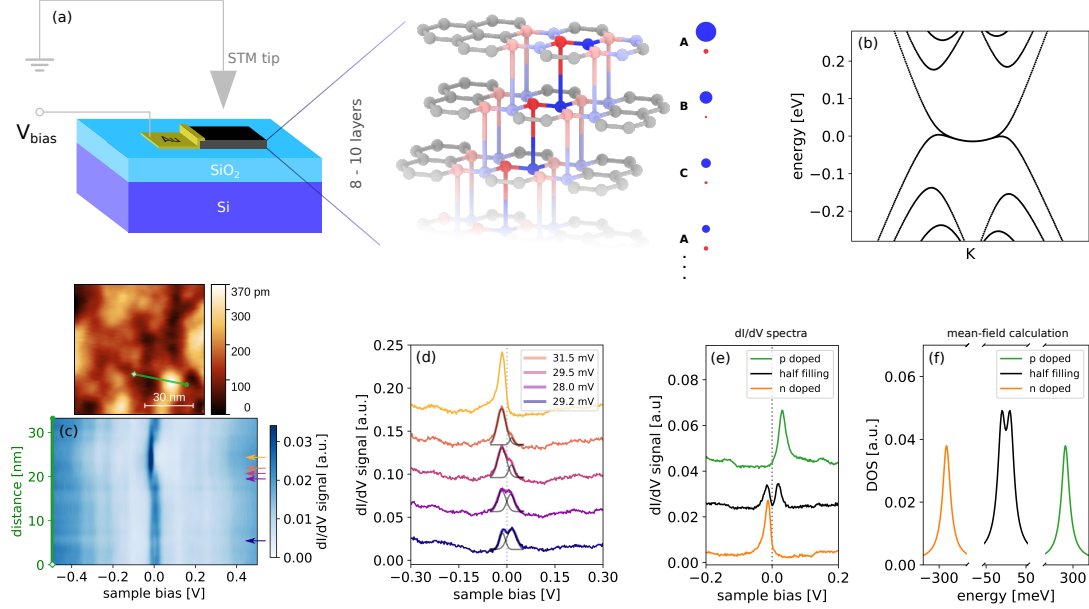


Figure 1: **Correlated insulating state in RG.** (a) Schematic of the STM measurement setup, with the RG supported on a SiO<sub>2</sub> substrate. Blue and red atoms/bonds, show the staggered, SSH-like<sup>25</sup> chain in RG<sup>24</sup>. Nearest neighbor chains, shown in lighter blue and red colors form a ladder, through inter-chain hoppings. The size of the blue and red circles next to the graphene layers is proportional to the LDOS on the respective sublattices. A, B and C mark the characteristic stacking pattern of RG. (b) Calculated ab-initio band structure of RG around the K point, for 8 layers. (c) Density plot of 64  $dI/dV$  spectra measured along the green line shown in the STM topography image above (8 layer sample). The surface state shifts in energy from being at the Fermi level to being almost completely filled and back to half filling. (d) Selected spectra, positions shown by arrows of the same color as in (c). The splitting in the surface state is always at the Fermi level, shown by the dotted line. Black Gaussians are fits to the surface state  $dI/dV$  peak, with a splitting shown in the inset. (e)  $dI/dV$  spectra measured in various positions on the sample surface, with the surface state below (orange), above (green) and at the Fermi level (black). The surface state shows a splitting of 32 meV at charge neutrality (black). The FWHM of the completely filled or empty surface state is 26 meV. (f) Surface total DOS, calculated within the mean-field approach for various doping levels ( $U = 6$  eV). Colors with the same meaning as in (e).

## Gapped and gapless domains at charge neutrality

We have used Raman spectroscopy to identify thick RG samples on a  $\text{SiO}_2$  support (for details see SI1) and performed STM measurements at multiple locations on an 8, 10 and 17 layer sample. The data presented in the main text is representative of the behavior seen in all samples. A topographic image of an  $80 \times 80$  nm area of the 8 layer thick sample is shown in Figure 1c, while the large density of states of the surface flat band shows up as a pronounced peak in the  $dI/dV$  spectra (Fig. 1c,d,e). The RG sample is subjected to the local charge and mechanical deformation inhomogeneity of the  $\text{SiO}_2$  support. It is well known that this modulates the doping in the sample placed on top<sup>38</sup> and we use this inhomogeneity to our advantage. By simply moving the STM tip over the sample we are able to investigate the surface state at various electron fillings.

Figure 1c, shows spectra across a 35 nm long line on the surface. The surface state suffers a local shift across the Fermi level (zero bias), with selected spectra shown in 1d. We observe a  $\sim 30$  meV splitting, centered on zero bias as soon as the surface state becomes partially filled with electrons, which is a strong indication of its many-body origin. In Fig. 1e, we highlight the three representative cases, with the surface state at charge neutrality (black), filled (orange) and empty (green). In the latter two situations, the full width at half maximum (FWHM,  $w$ ) is 26 meV, which reproduces the 25 meV bandwidth from ARPES measurements<sup>39</sup> and our ab-initio calculations (Fig. 1b). The filled and empty peaks show a shoulder on the right and left sides respectively. This asymmetry is characteristic of the doped spectra, similarly to "magic angle" bilayers, indicating that e-e interactions are present even at near complete filling of the band<sup>32;35</sup>. At half filling, the  $dI/dV$  peak shows a splitting of 32 meV. To reveal the origin of the observed peak splitting we have performed calculations at the mean-field level, evidencing the opening of a gap due to antiferromagnetic exchange<sup>17</sup> (see Fig. 1f and SI2.3 for details). We have checked that quantum confinement effects due to the local doping profiles and possible local electric fields fail to reproduce the observed splitting (see SI7).

Next, we have quantified the local variation of the splitting over large areas of the sample surface. Figure 2a is a representative example of this, with more splitting maps, as well as the

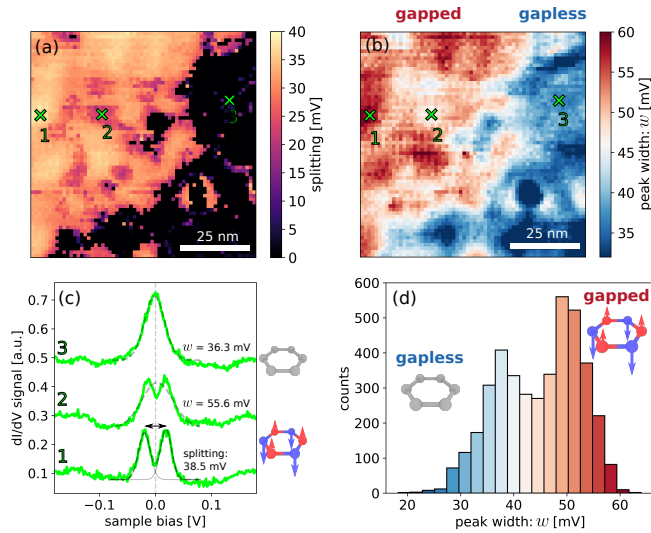


Figure 2: **Gapped and gapless domains.** (a) Map of the surface state splitting over an  $80 \times 80$  nm area of the sample, measured using a grid of  $64 \times 64$   $dI/dV$  spectra. The splitting was determined by fitting two Gaussians to the peak. Examples of fits can be seen in (c) and Fig. 1d. (b) FWHM ( $w$ ) of the peak from the same  $dI/dV$  map, obtained by fitting a single Gaussian (for fitting details see SI4). (c) Examples of individual  $dI/dV$  spectra measured in locations shown by numbers on (a) and (b). Double and single Gaussian fits shown by gray dashed curves, the splitting and  $w$  values shown next to the spectra. (d) Histogram of peak widths ( $w$ ) in the data of (b). Tip stabilization parameters: 100 pA, 500 mV.

details of the fitting procedure shown in SI4 and SI5. One striking feature of the map is that the sample contains regions with no observable splitting, even though the flat band is half filled in most of the area, as illustrated by spectrum #3 in Fig. 2c (see also supplementary Fig. S7). This is surprising at first, since the mean-field ground state in tri- and tetra-layers is gapped<sup>17;20;22</sup>. The presence of a gapless surface density indicates the failure of the mean-field approximation to fully capture the behavior of 8 layer RG.

The domain structure is also apparent if we fit a single Gaussian to the spectra and plot the FWHM  $w$ , which shows a bimodal distribution (Fig. 2d). Furthermore, the peak width in the areas without splitting is at least 10 mV larger than in the fully doped case, suggesting that many-body effects do play a role in this case. We call the areas without splitting: gapless, up to the energy resolution of our measurement, meaning that we can not rule out the presence of a gap smaller than 4.5 meV. In the measurements, slight deviation from charge neutrality, but with the Fermi levels still near half filling, does not alter the gapped or gapless nature of the

peak, as can be seen in Fig. 1d and in the supplementary Fig. S7.

## Degenerate ground state in RG and the breakdown of the mean-field approximation

The dual nature of the flat band charge density is remarkable, since at the mean-field level, gapless ground states are not expected to be stable<sup>36</sup>. The DMRG approach goes beyond the mean-field approximation and allows us to compute the complete many-body wave function, taking quantum fluctuations fully into account that are crucial in low-dimensional systems. Fig. 3a shows the magnetic moments on the top four graphene layers along a staggered chain of RG, calculated using DMRG. The local moments show an antiferromagnetic ordering on the graphene sublattices, which decay into the bulk to near zero by the third graphene layer. It can be seen that the mean-field calculations also reproduce this sublattice-Néel magnetic ordering, where the total spin for one surface,  $s_z$  within the RG unit cell is 1. When mapping the local density of states (LDOS) of the top graphene layer by STM, this Néel ordering results in an insulating state, with a splitting shown in Fig. 1f. One expects an insulator, because the magnetic ordering breaks the inversion and time reversal symmetries protecting the gapless state at charge neutrality<sup>40</sup>, resulting in the splitting observed in STM.

Beyond the agreement on the magnetic ordering, we find that the mean-field approach overestimates the ground state energy of RG by 5.16 meV/atom compared to the DMRG result, highlighting the importance of correlation effects in the system (for more details see SI2). In DMRG calculations the ground state of the RG slab features spins localized to the bottom and top layers, with a total spin of  $\mathcal{S}_T$  and a spin projection of  $\mathcal{S}_{T,z}$ . In Fig. 3b we plot the ground state energies, as a function of the two-site approximation of the full variance  $v$ , defined by  $v = \langle H^2 \rangle - \langle H \rangle^2$ , where  $H$  is the Hamiltonian and  $\langle \dots \rangle$  denotes the expectation value with respect to the variational state. Three different configurations of the total spin,  $\mathcal{S}_T = 0, 1, 2$  converge to the exact ground state at  $v = 0$ , all of them being degenerate. Since in STM we are probing only one surface, these total spin states correspond to three possible spin projections on the top surface:  $s_z = 0, \pm 1$ . Among these, the  $s_z = \pm 1$  (Néel) also features in the mean-field result, with the +1 state shown in Fig. 3c and the -1 state corresponding to the case, where

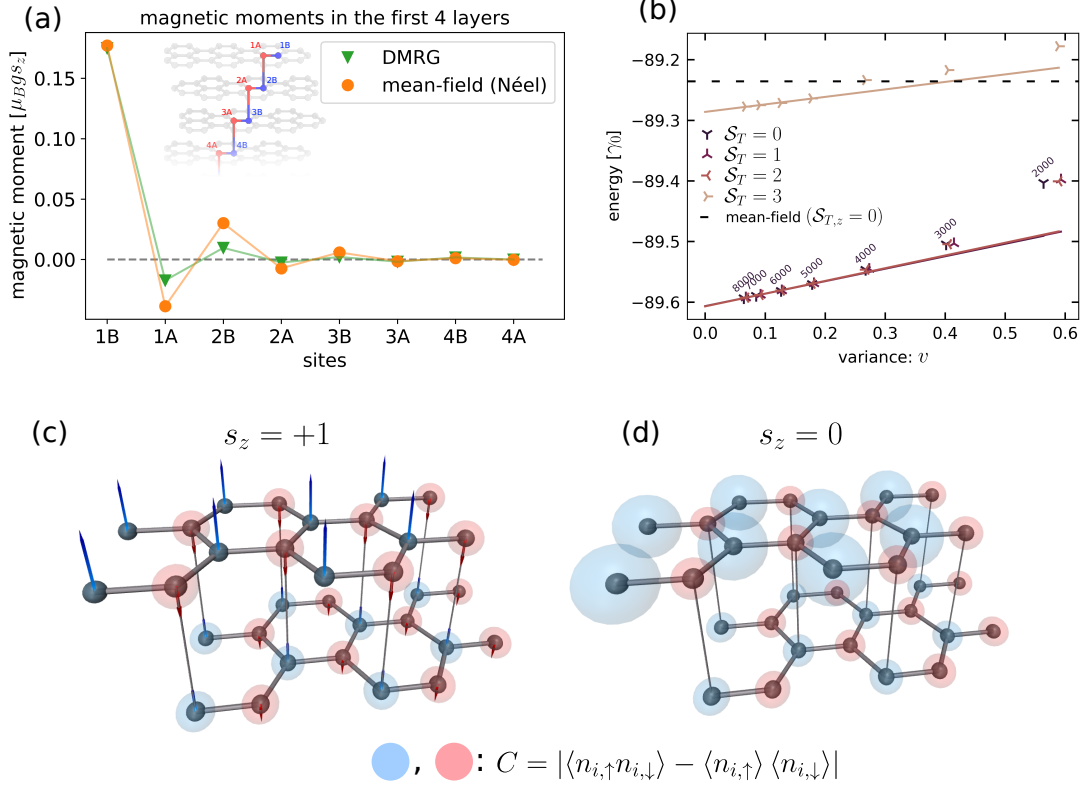


Figure 3: **DMRG and mean-field Hubbard model calculations.** (a) Calculated local magnetic momenta for a 6 layer RG. The magnetic moments on the atomic sites decay exponentially, essentially to zero after the second graphene layer ( $U = 0.5 \times \gamma_0$ ). Inset shows one staggered chain of RG in red and blue atoms, along which the plot is performed. (b) DMRG calculations of the ground states of a 6 layer thick cell as a function of the variance. Energy in units of the nearest neighbor hopping term:  $\gamma_0$ . The exact ground state is reached at zero variance. The states with various total spin of whole cell (both top and bottom graphene layers):  $S_T$  are degenerate, with a ground state that is 5.16 meV/atom smaller than the mean-field case (dashed line). The first excited spin state ( $S_T = 3$ ) is  $0.33 \times \gamma_0$ . (c, d) Colored arrows showing the distribution of magnetic moments on the top two graphene layers with a surface spin of  $s_z$ , from the DMRG calculation. The magnetic moments  $\mu$  are scaled by  $2|\mu|^{1/4}$ , for better visibility. The radius of the opaque spheres is proportional to the local electronic correlation  $C$  values, as defined by the relation shown.  $\langle n_{i,\uparrow} \rangle$  and  $\langle n_{i,\downarrow} \rangle$  are the expectation values of the spin density on the atomic site  $i$ . Blue and red colors distinguish the two graphene sublattices.



the spins are inverted. These two states are indistinguishable if the STM tunneling current is not spin polarized. However, the  $s_z = 0$  instance has no analogue in the mean-field approximation, since the mean-field decoupling excludes the possibility to host a correlated state and only magnetic solutions can result in a lower energy. This correlation effect is shown in Fig. 3c and d, where the radius of the colored spheres is proportional to the calculated charge correlation values ( $C$ ). Instead of the magnetic moments, the  $s_z = 0$  solution shows an enhanced local charge correlation on the unpaired sublattice, forming a correlated paramagnet on the surface. In this state the charge fluctuations are more and more suppressed with increasing  $U$  (the electrons prefer not to hop to already occupied sites) and the total energy is decreased directly by the smaller number of doubly occupied sites instead of long-range magnetic ordering. This is a truly many-body effect, since the mean-field approach is only able to decrease the total energy via magnetic ordering and not by decreasing the doubly occupied sites. This state is gapless for the charge degree of freedom, since there is no large scale breaking of symmetries<sup>40</sup>, as opposed to the  $s_z = \pm 1$  case. The two degenerate states form a natural candidate for the domain structure observed in STM, with a gapped antiferromagnetic insulator and a gapless, correlated paramagnet. Globally over the whole sample surface none of the two states can dominate, but locally due to inhomogeneities the system can favor either the  $s_z = \pm 1$  or the  $s_z = 0$  state, similarly to competing states in strongly correlated materials<sup>31</sup>.

Finally, we have calculated the energy of the  $\mathcal{S}_T = 3$  state and find that it is  $0.33 \times \gamma_0$  higher than the ground state for a 6 layer thick cell (Fig. 3b), with  $\gamma_0$  being the nearest neighbor hopping of graphene. This gap separates, the first (bulk) excited spin state of RG, from the degenerate ground state. The large size ( $\sim 1$  eV) of the spin gap is responsible for the rapid decay of the magnetic moments ( $s_z$ ) at the top and bottom graphene layers.

## Critical temperature

Having established the presence of correlated insulating and gapless phases, we have checked their temperature dependence. In Fig. 4a and b, we show another example of the domain structure of the surface state splitting. By measuring the same  $80 \times 80$  nm area of the sample at increasing temperature, we observe that the splitting and  $w$  suddenly decreases at a temperature

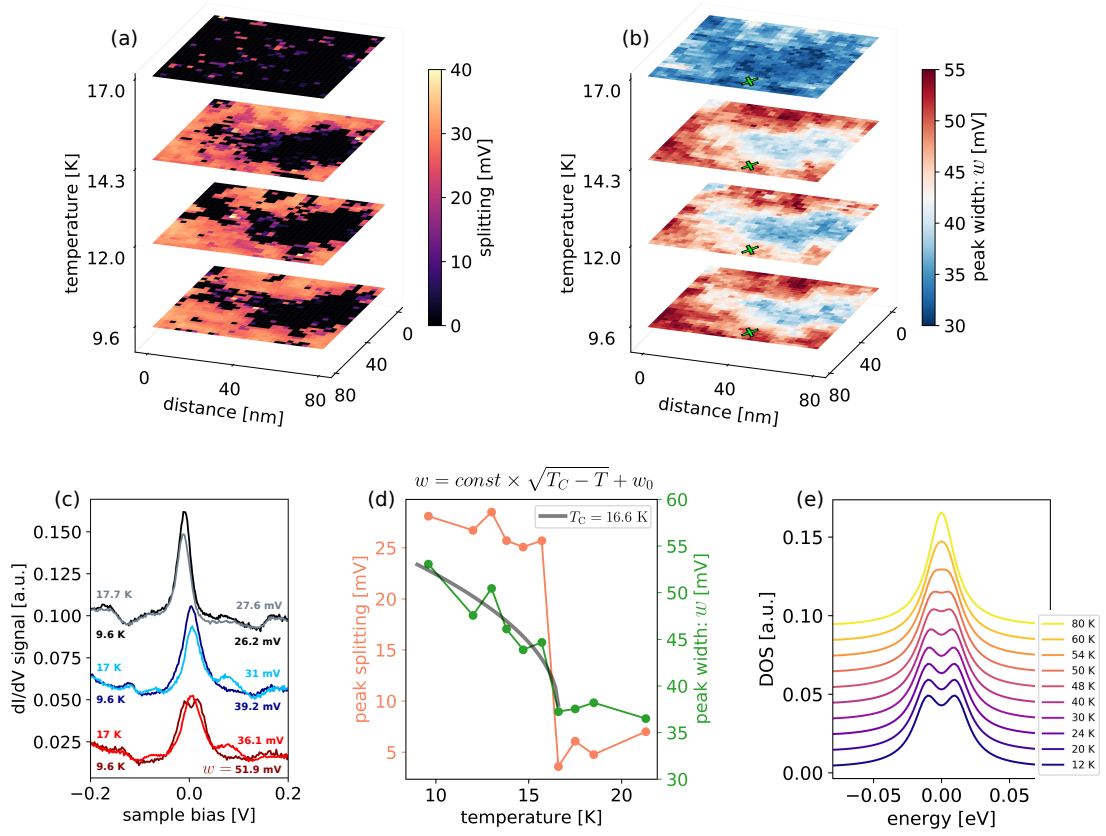


Figure 4: **Temperature dependence.** (a) Map of the surface state splitting in an  $80 \times 80$  nm area on the 8 layer sample. The same area is measured at four different temperatures. (b) Map of  $w$  in the same area and temperatures as in (a). Above 16.6 K, the splitting vanishes and the peak width decreases sharply. (c) Selected spectra in a gapped (bottom), gapless (middle) and completely filled (top) area below and above the critical temperature. The width:  $w$  of the peaks shown in mV next to the spectra. Spectra at different temperatures are measured in the same location. (d) Peak splitting (orange) and  $w$  of the surface state (green) as a function of temperature, measured in the position marked by the green crosses in (b). Gray line is a fit to  $w$  below  $T_C$ , using the function shown. Connecting lines are guide to the eye. (e) Temperature dependent mean-field calculation of the splitting at charge neutrality ( $U = 6$  eV).

of 17 K all across the surface. Example spectra are shown in Fig. 4c in a gapped (red) and a gapless (blue) region, measured at different temperatures in the same surface position. Raising the temperature from 9.6 K to 17 K, the surface state becomes a single peak with decreasing  $w$ . This is in contrast to a highly doped area (gray spectra), where  $w$  increases by 1.4 mV, corresponding to the extra broadening due to the increased temperature (see also Fig. S10).

This suggests the presence of a phase transition at charge neutrality. Focusing on the gapped state, the size of the splitting and therefore the width of the peak is proportional to the magnetization of the sample, therefore  $w$  is a measure of the order parameter. Below  $T_C$  we find that  $w$  shows a behavior consistent with a second order phase transition, by fitting it with the function:  $w = const \times \sqrt{T - T_C} + w_0$ , with  $w_0 = 37.5$  mV being the peak FWHM above  $T_C$ . Critical temperature values measured on different areas of the sample show a variation. The value of  $T_C$  for the area shown in Fig. 4 is 16.6 K, with the highest  $T_C$  measured to be 20 K (see SI6). Above  $T_C$ , the  $dI/dV$  peak width is still roughly 10 meV wider than the  $w$  expected from single particle band structure (26 meV), suggesting that some many-body effects might still play a role at these temperatures. Our temperature dependent mean-field calculation reproduces the narrowing of the peak by increasing temperature, but as expected, it overestimates  $T_C$  (Fig. 4e).

Having determined the bandwidth and critical temperature in RG, it is instructive to compare it to the correlated insulator observed in "magic angle" twisted bilayer graphene at half filling of the superlattice flat band. As a rule of thumb, the strength of interactions scales with the inverse bandwidth, measured by STM in twisted bilayers as the 10-13 meV FWHM of the LDOS peak<sup>32</sup>. This bandwidth is associated with a splitting of 6.5 meV<sup>32</sup>, and a metal-insulator transition at 4 K<sup>41</sup>. Even though the bandwidth in RG is twice as large as in twisted bilayers, the splitting and critical temperature we observe is five times larger, indicating much stronger interactions in RG.

## Symmetry breaking away from charge neutrality

We now turn our attention to the situation when the surface state is away from charge neutrality, but not completely doped. Mean-field calculations at slight ( $2.16 \times 10^{12}$  cm<sup>-2</sup>, Fig. 5b) doping suggest that the gap closes, but the surface magnetization does not vanish. Instead it forms a

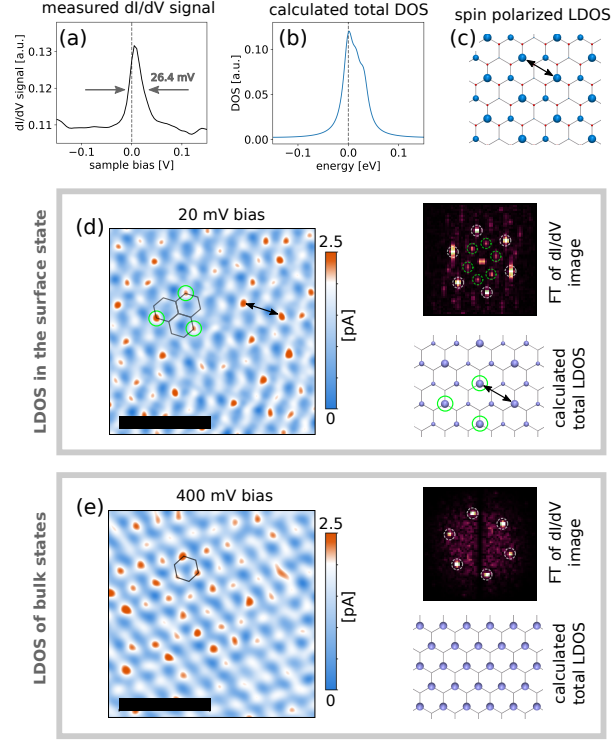


Figure 5: **Ferromagnetism and spontaneous breaking of translational symmetry.** (a)  $dI/dV$  spectrum measured in an area with slight  $p$  doping. FWHM,  $w$  of the surface state peak is 26.4 mV. (b) DOS for  $p$  doping of  $2.16 \times 10^{12} \text{ cm}^{-2}$ , similar to the experiment, calculated by the mean-field model. (c) Mean-field calculation of the spin resolved LDOS of the top layer of  $p$  doped RG. Size of circles is proportional to the LDOS of the top graphene layer in the flat band ( $U = 4.2 \text{ eV}$ ). The LDOS shows essentially a ferromagnet, blue: up spin, red: down spin. Black arrow marks the  $\sqrt{3} \times$  enlarged unit cell size. This magnetization pattern is also reproduced in DMRG. (d) STM image of the  $dI/dV$  signal inside the surface state. Black arrows and green circles show the enlarged unit cell size. Stabilization parameters: 30 pA, 20 mV. (e)  $dI/dV$  image far from the surface state. Stabilization parameters: 300 pA, 400 mV. Insets in (d), (e): Fourier transform of the  $dI/dV$  image. White, dashed circles show the atomic periodicity corresponding to the  $2.46 \text{ \AA}$  unit cell of graphene. Green circles show the unit cell of  $2.46 \times \sqrt{3} \text{ \AA}$ . Size of blue spheres is proportional to the calculated total LDOS in the flat band: (d) and 240 meV above the flat band: (e). Scale bars on the  $dI/dV$  images are 1 nm in length. Stabilization parameters in (d) and (e) are chosen, such that the tip - sample distance stays the same. Measurement temperature was 9.6 K.

ferromagnetic pattern with a  $(\sqrt{3} \times \sqrt{3})R30^\circ$  enlarged unit cell (Fig. 5c). At this doping, mean-field calculations suffice, since we are dealing with a magnetic state. Nevertheless, we have checked that DMRG calculations also reproduce this enlarged unit cell and the magnetizations agree well with the mean-field ones. Interestingly, this translation symmetry breaking is also present in the total LDOS, which is the quantity that is measured by STM. Indeed, the image of the  $dI/dV$  signal inside the surface state at 20 mV, shows the enlarged unit cell, both in the graphite lattice and in the Fourier transform of the data (Fig. 5d). Measuring at a bias voltage well outside the surface state, in the same area of the sample, simply shows the expected periodicity of graphite (Fig. 5e).

Ferromagnetism has been predicted at finite doping<sup>42</sup> and recently measured in the compressibility of trilayer RG<sup>43</sup>. Our results suggest that ferromagnetism is also present in thick RG, and is accompanied by translation symmetry breaking. At present it is still unclear whether the interaction induced  $\sqrt{3} \times \sqrt{3}$  instability is accompanied by the formation of a Kekulé gap<sup>44–46</sup>, or some other valley order<sup>37</sup>.

## Concluding remarks

We have shown that interactions in the surface state of thick RG produce a ground state that is fundamentally different from the mean-field prediction, having a domain structure of gapped and gapless surface charge density. According to our DMRG calculations this domain structure is a result of the degenerate ground state. The fundamental difference between 3 to 4 layers and thick samples is that in the latter the surface states on opposite graphene terminations do not overlap<sup>30</sup>. Such an overlap changes the nature of the quantum magnet and lifts the characteristic degeneracy, resulting in a completely gapped ground state, as recently shown in triangulene molecules<sup>7</sup>. As a consequence, the surface charge density in tetra-layers is always gapped and magnetic, therefore it is well described by mean-field theory<sup>22</sup>. Perhaps most importantly, RG provides a platform for the straightforward tuning of the correlated phase discussed here, through electric and magnetic fields<sup>30</sup> and by mechanical strain, in a simple defect free quantum material.

Our DMRG calculations show that at charge neutrality, the spin and charge interactions

in RG result in a degenerate ground state and a bulk spin gap. These properties are also shared by a simpler toy model, the 1D quantum spin chain with a bulk spin of 2<sup>1;47</sup>, raising the question: what other properties of this famous toy model are shared by RG? Further theoretical and experimental investigations exploring the properties of this new system hold the promise of revealing the existence of non-local topological order, spin or charge fractionalization<sup>7;47;48</sup> and perhaps unconventional superconductivity<sup>49;50</sup>.

## Methods

STM measurements were done using an RHK PanScan Freedom microscope, at a temperature of 9.6 K, in ultrahigh vacuum at a pressure better than  $5 \times 10^{-11}$  Torr. STM tips were prepared by mechanically cutting Pt/Ir (90%/10%) wire.  $dI/dV$  spectra were measured using a Lock-In amplifier, with a bias modulation of 1.3 kHz and a modulation amplitude of 2 mV, for spectra with the highest energy resolution and for checking the presence of a gap in the gapless phase. We used a bias modulation of 10 mV for all  $dI/dV$  maps. The sample temperature was varied from 9 K to 30 K, using a resistive heater, with the temperature sensor located next to the sample holder. After setting a new measurement temperature, we let the temperature stabilize and corrected for thermal drift of the sample, by imaging the topography. By this procedure we were able to measure the  $dI/dV$  spectra at various temperatures in the same location on the sample.

## Acknowledgements

The work was conducted within the framework of the Topology in Nanomaterials Lendulet project, Grant No. LP2017-9/2/2017, with support from the European H2020 GrapheneCore3 Project No. 881603. LT acknowledges support from the Elvonal grant KKP 138144. TZ acknowledges support from the UNKP-20-4 New National Excellence Program of the Ministry for Innovation and Technology through NKFIH. PV and LO acknowledges the support of the Janos Bolyai Research Scholarship and LO for the Bolyai+ Scholarship of the Hungarian Academy of Sciences. JK and LO acknowledges the support of Ministry of Innovation and Technology of Hungary within the Quantum Information National Laboratory.

## Author contributions

MSMI prepared and characterized the sample. STM measurements were performed by MSMI, KK and PNI. IH designed and performed the DMRG and mean-field calculations, ZT and PV provided the various tight-binding Hamiltonians. KM, PK and AP were involved in the Raman spectroscopic mapping and sample preparation. ZT performed the ab-initio calculations, under the supervision of JK with the assistance of PV. OL and AA performed the tight-binding modelling of quantum confinement effects. LT contributed to data analysis. PNI conceived and coordinated the project and wrote the manuscript with input from all authors.

## References

- [1] Haldane, F. D. M. Nonlinear field theory of Large-Spin heisenberg antiferromagnets: Semiclassically quantized solitons of the One-Dimensional Easy-Axis n\`eel state. *Phys. Rev. Lett.* **50**, 1153–1156 (1983).
- [2] Dagotto, E. & Rice, T. M. Surprises on the way from one- to Two-Dimensional quantum magnets: The ladder materials. *Science* **271**, 618–623 (1996).
- [3] Schollwöck, U., Richter, J., Farnell, D. J. J. & Bishop, R. F. (eds.) *Quantum Magnetism* (Springer, Berlin, Heidelberg, 2004).
- [4] Vasiliev, A., Volkova, O., Zvereva, E. & Markina, M. Milestones of low-d quantum magnetism. *npj Quantum Materials* **3**, 1–13 (2018).
- [5] Magda, G. Z. *et al.* Room-temperature magnetic order on zigzag edges of narrow graphene nanoribbons. *Nature* **514**, 608–611 (2014).
- [6] Just, S. *et al.* Preferential antiferromagnetic coupling of vacancies in graphene on SiO<sub>2</sub>: Electron spin resonance and scanning tunneling spectroscopy. *Phys. Rev. B: Condens. Matter Mater. Phys.* **90**, 125449 (2014).
- [7] Mishra, S. *et al.* Observation of fractional edge excitations in nanographene spin chains. *Nature* **598**, 287–292 (2021).

- [8] Lemonik, Y., Aleiner, I. & Fal'ko, V. I. Competing nematic, antiferromagnetic, and spin-flux orders in the ground state of bilayer graphene. *Phys. Rev. B Condens. Matter* **85**, 245451 (2012).
- [9] Lang, T. C. *et al.* Antiferromagnetism in the hubbard model on the bernal-stacked honeycomb bilayer. *Phys. Rev. Lett.* **109**, 126402 (2012).
- [10] Young, A. F. *et al.* Spin and valley quantum hall ferromagnetism in graphene. *Nat. Phys.* **8**, 550–556 (2012).
- [11] Young, A. F. *et al.* Tunable symmetry breaking and helical edge transport in a graphene quantum spin hall state. *Nature* **505**, 528–532 (2013).
- [12] Sharpe, A. L. *et al.* Emergent ferromagnetism near three-quarters filling in twisted bilayer graphene. *Science* **365**, 605–608 (2019).
- [13] Chen, G. *et al.* Tunable correlated chern insulator and ferromagnetism in a moiré superlattice. *Nature* **579**, 56–61 (2020).
- [14] Vancsó, P., Hagymási, I. & Tapasztó, L. A magnetic phase-transition graphene transistor with tunable spin polarization. *2D Mater.* **4**, 024008 (2017).
- [15] Velasco, J. *et al.* Transport spectroscopy of symmetry-broken insulating states in bilayer graphene. *Nat. Nanotechnol.* **7**, 156–160 (2012).
- [16] Geisenhof, F. R. *et al.* Quantum anomalous hall octet driven by orbital magnetism in bilayer graphene. *Nature* **598**, 53–58 (2021).
- [17] Lee, Y. *et al.* Competition between spontaneous symmetry breaking and single-particle gaps in trilayer graphene. *Nat. Commun.* **5**, 5656 (2014).
- [18] Yankowitz, M. *et al.* Electric field control of soliton motion and stacking in trilayer graphene. *Nat. Mater.* **13**, 786–789 (2014).
- [19] Hattendorf, S., Georgi, A., Liebmann, M. & Morgenstern, M. Networks of ABA and ABC stacked graphene on mica observed by scanning tunneling microscopy. *Surf. Sci.* **610**, 53–58 (2013).



- [20] Myhro, K. *et al.* Large tunable intrinsic gap in rhombohedral-stacked tetralayer graphene at half filling. *2D Materials* **5**, 045013 (2018).
- [21] Lee, Y. *et al.* Gate tunable magnetism and giant magnetoresistance in ABC-stacked Few-Layer graphene (2019). 1911.04450.
- [22] Kerelsky, A. *et al.* Moiréless correlations in ABCA graphene. *Proc. Natl. Acad. Sci. U. S. A.* **118** (2021).
- [23] Pamuk, B., Baima, J., Mauri, F. & Calandra, M. Magnetic gap opening in rhombohedral-stacked multilayer graphene from first principles. *Phys. Rev. B Condens. Matter* **95**, 075422 (2017).
- [24] Min, H. & MacDonald, A. H. Electronic structure of multilayer graphene. *Progr. Theoret. Phys. Suppl.* **176**, 227–252 (2008).
- [25] Su, W. P., Schrieffer, J. R. & Heeger, A. J. Solitons in polyacetylene. *Phys. Rev. Lett.* **42**, 1698–1701 (1979).
- [26] Xiao, R. *et al.* Density functional investigation of rhombohedral stacks of graphene: Topological surface states, nonlinear dielectric response, and bulk limit. *Phys. Rev. B* **84**, 1–15 (2011).
- [27] Slizovskiy, S., McCann, E., Koshino, M. & Fal’ko, V. I. Films of rhombohedral graphite as two-dimensional topological semimetals. *Communications Physics* **2**, 164 (2019).
- [28] Nawa, K. *et al.* Triplon band splitting and topologically protected edge states in the dimerized antiferromagnet. *Nat. Commun.* **10**, 2096 (2019).
- [29] Le, N. H., Fisher, A. J., Curson, N. J. & Ginossar, E. Topological phases of a dimerized Fermi–Hubbard model for semiconductor nano-lattices. *npj Quantum Information* **6**, 1–10 (2020).
- [30] Shi, Y. *et al.* Electronic phase separation in multilayer rhombohedral graphite. *Nature* **584**, 210–214 (2020).

- [31] Dagotto, E. Complexity in strongly correlated electronic systems. *Science* **309**, 257–262 (2005).
- [32] Kerelsky, A. *et al.* Maximized electron interactions at the magic angle in twisted bilayer graphene. *Nature* **572**, 95–100 (2019).
- [33] Jiang, Y. *et al.* Charge order and broken rotational symmetry in magic-angle twisted bilayer graphene. *Nature* **573**, 91–95 (2019).
- [34] Choi, Y. *et al.* Electronic correlations in twisted bilayer graphene near the magic angle. *Nat. Phys.* **15**, 1174–1180 (2019).
- [35] Xie, Y. *et al.* Spectroscopic signatures of many-body correlations in magic-angle twisted bilayer graphene. *Nature* **572**, 101–105 (2019).
- [36] Jung, J. & MacDonald, A. H. Gapped broken symmetry states in ABC-stacked trilayer graphene. *Phys. Rev. B Condens. Matter* **88**, 075408 (2013).
- [37] Zhang, F., Jung, J., Fiete, G. A., Niu, Q. & MacDonald, A. H. Spontaneous quantum hall states in chirally stacked few-layer graphene systems. *Phys. Rev. Lett.* **106**, 156801 (2011).
- [38] Zhang, Y., Brar, V. W., Girit, C., Zettl, A. & Crommie, M. F. Origin of spatial charge inhomogeneity in graphene. *Nat. Phys.* **5**, 722–726 (2009).
- [39] Henck, H. *et al.* Flat electronic bands in long sequences of rhombohedral-stacked graphene. *Phys. Rev. B Condens. Matter* **97**, 245421 (2018).
- [40] Mañes, J. L., Guinea, F. & Vozmediano, M. A. H. Existence and topological stability of fermi points in multilayered graphene. *Phys. Rev. B: Condens. Matter Mater. Phys.* **75**, 155424 (2007).
- [41] Cao, Y. *et al.* Correlated insulator behaviour at half-filling in magic-angle graphene superlattices. *Nature* **556**, 80–84 (2018).
- [42] Olsen, R., van Gelderen, R. & Smith, C. M. Ferromagnetism in ABC-stacked trilayer graphene. *Phys. Rev. B Condens. Matter* **87**, 115414 (2013).

- [43] Zhou, H. *et al.* Half- and quarter-metals in rhombohedral trilayer graphene. *Nature* **598**, 429–433 (2021).
- [44] Weeks, C. & Franz, M. Interaction-driven instabilities of a dirac semimetal. *Phys. Rev. B Condens. Matter* **81**, 085105 (2010).
- [45] Roy, B. & Herbut, I. F. Unconventional superconductivity on honeycomb lattice: Theory of kekule order parameter. *Phys. Rev. B Condens. Matter* **82**, 035429 (2010).
- [46] Gamayun, O. V., Ostroukh, V. P., Gnezdilov, N. V., Adagideli, Í. & Beenakker, C. W. J. Valley-momentum locking in a graphene superlattice with y-shaped kekulé bond texture. *New J. Phys.* **20**, 023016 (2018).
- [47] Schollwöck, U. & Jolicoeur, T. Haldane gap and hidden order in the  $S = 2$  antiferromagnetic quantum spin chain. *EPL* **30**, 493 (1995).
- [48] Pollmann, F., Berg, E., Turner, A. M. & Oshikawa, M. Symmetry protection of topological phases in one-dimensional quantum spin systems. *Phys. Rev. B Condens. Matter* **85**, 075125 (2012).
- [49] Volovik, G. E. Flat band in topological matter. *J. Supercond. Novel Magn.* **26**, 2887–2890 (2013).
- [50] Zhou, H., Xie, T., Taniguchi, T., Watanabe, K. & Young, A. F. Superconductivity in rhombohedral trilayer graphene. *Nature* **598**, 434–438 (2021).